Nanoscale

PAPER

View Article Online
View Journal | View Issue

Check for updates

Cite this: *Nanoscale*, 2019, **11**, 22378

Inhibition of light emission from the metastable tetragonal phase at low temperatures in island-like films of lead iodide perovskites†

Raquel Chuliá-Jordán, *[a] Natalia Fernández-Delgado,[b] Emilio J. Juárez-Pérez, [c] Iván Mora-Seró, [c] Miriam Herrera,[b] Sergio I. Molina[b] and Juan P. Martínez-Pastor *[a]

Photonic applications based on halide perovskites, namely $CH_3NH_3PbI_3$ ($MAPbI_3$), have recently attracted remarkable attention due to the high efficiencies reported for photovoltaic and light emitting devices. Despite these outstanding results, there are many temperature-, laser excitation power-, and morphology-dependent phenomena that require further research to be completely understood. In this work, we have investigated in detail the nature of exciton optical transitions and recombination dynamics below and above the orthorhombic/tetragonal ('O'-/'T'-) temperature phase transition (~150 K) depending on the material continuity (continuous-like) or discontinuity (island-like) in $MAPbI_3$ films. At low temperatures, continuous thin films of the perovskite can exhibit strain inhomogeneities associated with the formation of different 'T'-defective domains leading to an energy spread of states over more than 200 meV. On the other hand, a single photoluminescence line peak related to the perovskite 'O'-phase (associated with the distortion of the $[PbI_3]^-$ anion) is observed in the island-like sample that we attribute to strain relaxation for this morphology. Moreover, the predominantly radiative recombination dynamics of the continuous-like sample mainly originates from nongeminate electron–hole formation of excitons in the 'O'-phase and the internal dynamics with carrier trapping levels. This observation is in strong contrast to the free exciton recombination dominantly found in the island-like sample.

Received 1st September 2019,
Accepted 2nd November 2019

DOI: 10.1039/c9nr07543g

rsc.li/nanoscale

1. Introduction

Despite the great achievements in photovoltaics, as well as in photonics,[1–3] an efficient room-temperature compact hybrid plasmonic nanostructure, which might enable active functionalities in photonic and plasmonic circuitry, has yet to be developed. Latest studies suggest that a new candidate is required that would not just allow the construction of plasmon waveguides with highly concentrated light fields and very low propagation losses, but could be integrated on a silicon substrate. Most of the QD-based nanomaterials need femtosecond pulsed laser excitation to achieve population inversion due to the important non-radiative Auger losses (≈10 ps) observed, while organic materials display poor heat conductivity, limited wavelength tunability and bleaching (see introduction in ref. 4 and others therein). Recently, amplification of the spontaneous emission (ASE) has been observed in optimized hybrid lead halide perovskite-poly(methyl methacrylate) ($MAPbI_3$-PMMA) waveguides on a silicon architecture, because the losses were compensated for along the entire waveguide due to a weak attenuation of the pump under end-fire coupling. Furthermore, the high confinement of light in this photonic structure was the origin of a threshold for ASE as low as 30 μW inside the waveguide and a net gain of 10 dB cm^{-1} was obtained in waveguides 1 mm long.[4] These results suggest that $MAPbI_3$ perovskites could also be future aspirants for Si-hybrid photonics that might open up an avenue towards tightly integrated photonic and plasmonic circuits.

Important efforts in this direction have been made by different research groups. The perovskite material, which does not seem to present any significant disorder-induced broadening as inferred from the low Urbach energy measured (slope ≈ 15 meV), will not suffer from the Staebler–Wronski effect,[5] as occurs in amorphous silicon.[6,7] A reduction of the exciton binding energy from *ca.* 15 to 5 meV has been reported, for all the spectra above the orthorhombic/tetragonal ('O'-/'T'-) phase transition temperature, T_C (160 K).[8] This result is consistent with recent estimations, in which a decrease from 29 ± 6 to

---

[a] *Instituto de Ciencia de los Materiales, Universitat de València, C/Catedrático J. Beltrán, 2, Paterna 46980, Spain. E-mail: raquel.chulia@uv.es, martinep@uv.es*
[b] *Department of Material Science, Metallurgical Engineering and Inorganic Chemistry IMEYMAT, University of Cadiz, Spain*
[c] *Institute of Advanced Materials (INAM), Universitat Jaume I, 12071 Castelló, Spain*

† Electronic supplementary information (ESI) available. See DOI: 10.1039/c9nr07543g

13 ± 5 meV has been recently reported.[9] Hence, a certain portion of free electron–hole pairs will be in thermal equilibrium with excitons in $MAPbI_3$ at room temperature since the exciton binding energy is smaller than k_BT (~26 meV).[8] On the other hand, not only a contradictory exciton binding energy of 62.3 meV, extracted from photoluminescence (PL) intensity quenching at high temperatures, but also the appearance of a PL band ascribed to $MAPbI_3$ in its tetragonal phase subsisting below T_C has been reported.[10] Lastly, it has been proved that although the relative volume fraction of low-energy states (inclusions of crystallites with the tetragonal phase) is very small, they provide the dominant radiative recombination path, as compared to the states of the 'O'-phase that can be also observed in the PL spectra.[11] More recently, in a very nice study, Jones and co-workers[12] demonstrated a linear correlation between compressive strain measured locally (grains of the $MAPbI_3$ polycrystalline film) and the increase of the relative defect density contributing to carrier non-radiative losses. The latter relation is still an open question, but the appearance of strain-related defects is probably due to the particular solution processing conditions to form $MAPbI_3$ films (in the cubic phase at 100 °C, as compared to the tetragonal phase at room temperature).

In the present work we have analysed the influence of the film morphology (continuous-/island-like) and underlying crystalline ('O'-/'T'-) structure of the $MAPbI_3$ layer on the energy spread of states below the intrinsic excitonic optical transitions. To that end, we have studied in detail these optical transitions and their recombination dynamics below and above the 'O'-/'T'- phase transition temperature under different fluence excitation conditions. This was done by using steady-state and time-resolved PL spectroscopy. Remarkable changes in the exciton recombination are observed below and above T_C. Particularly interesting is the case of the island-like structures (island height of around 100 nm) where a single narrow PL line related to the $MAPbI_3$ 'O'-phase is dominant below 160 K. This behaviour can be attributed to the strain relaxation taking place in perovskite islands inhibiting the low energy PL bands associated with 'T'-phase crystallite inclusions (as a possible origin) at temperatures lower than T_C, as referred in the literature.[11] Therefore, our results demonstrate that future improvements in the growth of $MAPbI_3$ and other perovskite materials leading to the elimination of strain inhomogeneities will be fundamental to reduce the presence of carrier trapping centres below the bandgap and hence the basis to obtain high-performance optoelectronic, photonic and plasmonic devices based on perovskites.

2. Methods and materials

2.1. Sample preparation and description

The different steps of the growth process have been already explained in ref. 4 and 9. Briefly, the structure of the samples consists of a commercial Si/SiO_2 (2 μm) substrate, a TiO_2 compact layer (40 nm) deposited on it, whose mission is to enhance the residence time and adherence of the perovskite solution during the spin coating procedure, an active layer of $MAPbI_3$ and a poly-methyl methacrylate (PMMA) capping layer (0.5–1 μm) in order to protect the sample under ambient conditions (see Fig. 1). These materials were deposited by spin-coating at 2000 rpm for 60 s and post-processed at different heating temperatures and in air: TiO_2 at 500 °C for 30 min, $MAPbI_3$ at 100 °C for 1 h and PMMA with two heating steps at 80 and 150 °C for 2 min each. The two kinds of samples considered here, continuous and discontinuous or island-like films, have different average $MAPbI_3$ thicknesses, 550 and 100 nm, respectively. The different morphology is achieved by diluting the spin-casted perovskite solution from 40% (continuous thin film) to 10% (w/w) (island-like film). The samples for transmission electron microscopy (TEM) measurements were prepared in a conventional manner using ion-thinning (FISCHIONE, PIPs 691 GATAN). Given that the sample preparation could be affecting the structural quality of the perovskite layer under study, two different voltages for the ion milling processes were applied, 5 kV and 3–2.8 kV.

2.2. Experimental setup for PL experiments

Samples were characterized by placing them in the cold finger of a commercial closed-cycle compressed helium cryostat (ARS DE-202), where the temperature can be controlled from 10 K to room temperature. For excitation, a continuous wave laser diode at 405 nm was used for steady-state PL measurements, whereas a 200 fs pulsed Ti:sapphire laser (Coherent Mira 900D, 76 MHz repetition rate) doubled to 400 nm with a beta barium borate (BBO) crystal was used in time-resolved PL (TRPL) experiments. For detection, an Andor Newton 970 EMCCD camera (PL spectra) and a Si Micro Photon Device single photon avalanche diode (SPAD) photodetector (TR-PL spectra) were used. The SPAD was attached to a time correlated single photon counting electronic board (TCC900 from Edinburgh Instruments).[9,13,14]

3. Results and discussion

3.1. Morphological/structural properties

An accurate control of the morphology for each of the two different types of samples (continuous film and islands) is crucial[15–17] to exclude the random signals due to the surface morphology of spatially inhomogeneous samples. The SEM and TEM cross-section images can be seen in Fig. 1.

The High Angle Annular Dark Field-Scanning Transmission Electron Microscopy (HAADF-STEM) technique was used to obtain the high resolution information of both samples. The high-resolution interface images revealed the expected 2 μm thick SiO_2 film atop silicon (*i.e.*, substrate material), the 40 nm thick TiO_2 layer and the 550 nm thick $MAPbI_3$ continuous film (Fig. 1a (right-down)), which is polycrystalline with grains exhibiting a tetragonal structure. The HAADF-STEM technique also showed the 100 nm thick island-like $MAPbI_3$ (Fig. 1b (right-down)). The (near) cross-sectional Scanning Electron Microscopy (SEM) images of both polycrystalline perovskite

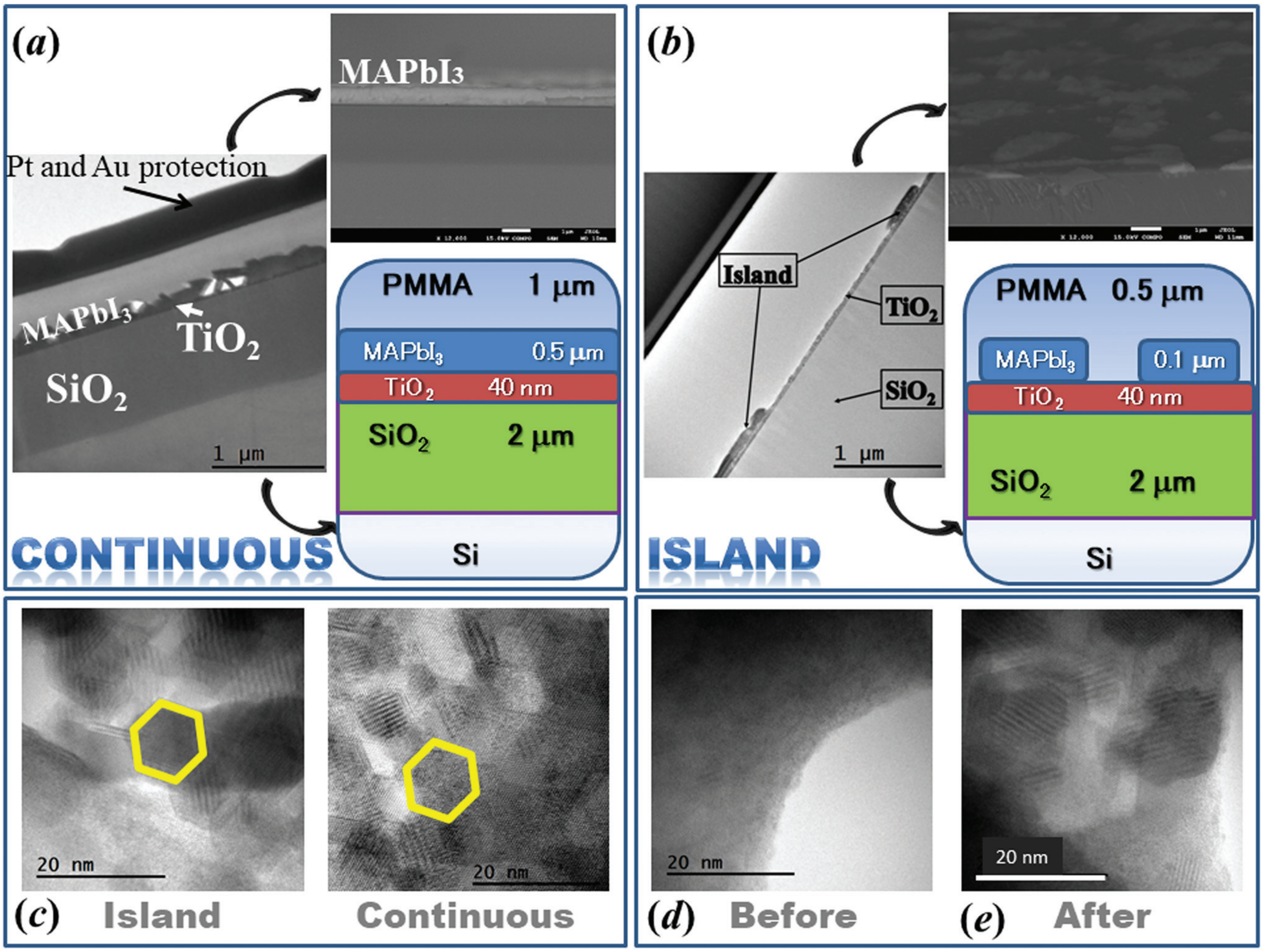

Fig. 1 Sample description: (a) HAADF-STEM (left) and SEM (right-up) cross-section images and structure (right-down) of the continuous-like perovskite (thickness 550 nm). The continuous-like perovskite is more compact; while in (b) the perovskite sample forms islands (thickness 100 nm–200 nm; size 1 μm). (c) Both perovskite samples are polycrystalline, where geometric crystals of a similar size have been observed at room temperature, mostly hexagons (as marked). Observation of the elimination of the material in the island-like (d) and continuous-like (e) sample after the study of the structure.

samples are shown in Fig. 1a and b (right-up). A more detailed study of the crystalline structure in both samples shows that the crystallites, in some areas, have defined geometric shapes, preferably a hexagonal shape (marked in the images of Fig. 1c) with an approximate size of about 10 nm. This short-range morphology has been observed both in the island-like (Fig. 1c-left) and continuous film (Fig. 1c-right) samples. The perovskite material ($MAPbI_3$) degrades under the electron beam, so that it may become amorphized.[18] In fact, when studying areas where $MAPbI_3$ is relatively thick, the "material" between crystalline zones is removed and, although at the beginning it is seen as a continuum (Fig. 1d), nm-size crystallites are later observed clearly (Fig. 1e). In other words, it seems that $MAPbI_3$ crystallites are embedded in some kind of amorphous perovskite material (Fig. 1d) that disappears under the electron beam irradiation, leaving the perovskite crystallites visible (Fig. 1e). It is important to note that neither the size of these crystallites nor their shape is modified after their continuous observation by TEM.

3.2. Optical properties: excitonic transitions

Optical characterization also offers local information (spatially averaged) despite the diffraction limit, given that photogenerated excitons are extended a few nanometers (*i.e.*, the effective Bohr radius of the exciton in the material) and act as a kind of optical probe. Fig. 2 shows different PL spectra acquired for the continuous thin film (a–c) and island-like (d–f) $MAPbI_3$ samples at different temperatures for several laser excitation powers. We observe clear differences in the PL spectra measured below T_C depending on the $MAPbI_3$ film morphology, continuous or island-like, especially under very low excitation conditions.

The PL band labelled as 'T' is located at around 783 nm (1.58 eV) at room temperature. It corresponds to the excitonic optical transition at the tetragonal phase of $MAPbI_3$ dominating above 150 K (see Fig. 2a–c).[11,19,20] The 'T'-band displays a weak intensity change and energy red-shift as the temperature decreases from 300 K to 150 K, as previously reported.[15] Below 150 K, a second PL band appears at ≈1.7 eV, for both continuous (see the PL spectra at 135 K in Fig. 2a–c) and island-like (see the PL spectrum at 140 K in Fig. 2d) samples, that exhibits a monotonous red shift with further decrease of the temperature (Fig. 2), being located at around 1.63 eV at 15 K. This PL band must be associated with $MAPbI_3$ at the 'O'-phase. In the range 150 K > T > 120 K, the PL bands associated with the 'T'- and 'O'-phases are coexisting; the first one ('T'-band) decreases in intensity, whereas the second ('O'-line peak) gains intensity with decreasing temperature. This behaviour reflects the phase transition from the tetragonal phase to the orthorhombic phase of the whole material. It is observed in both samples, even if T_C can be slightly lower in the case of the island-like sample.

It is important to mention now that the only dominant emission band at $T \approx 100$ K (95 and 96 K spectra in Fig. 2) is the one associated with the 'O'-phase in both samples. Below this temperature, a low energy emission band is observed below the 'O'-phase emission line, but only in the continuous-like sample. It is labelled as 'DT' in Fig. 2a–c. This broad and structured emission band ('DT') dominates over the 'O'-line peak for the lowest excitation power. In the literature, these 'DT'-bands have been attributed to different local strain conditions of the $MAPbI_3$ film leading to different transition temperatures,[10,11,21] but also to donor–acceptor pair (DAP) recombination behaviour.[15] In fact, up to four 'DT'-components appear in the PL spectra registered at the lowest laser fluencies that are extended more than 200 meV below the 'O'-line peak, as shown in Fig. 3a, but this extension decreases by

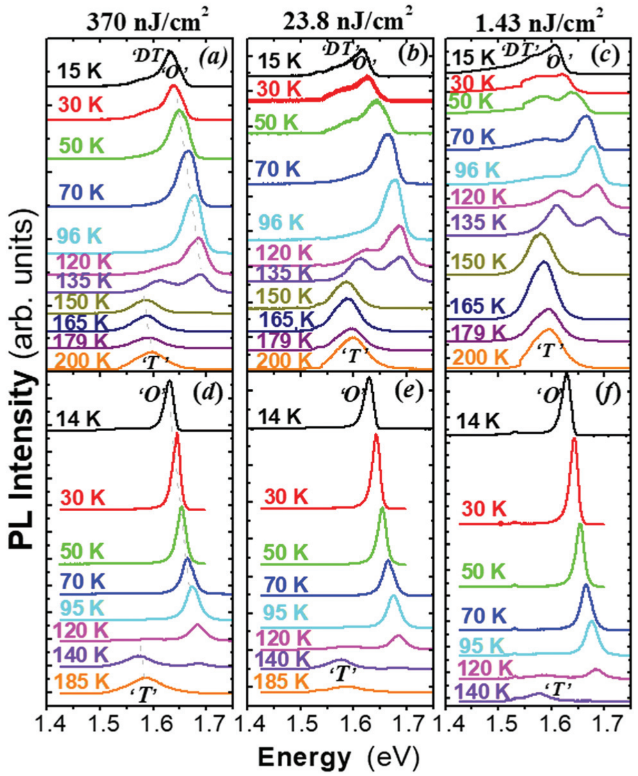

Fig. 2 Steady state PL spectra of the thin continuous-like (a–c) and island-like (d–f) perovskite at various temperatures and laser excitation powers.

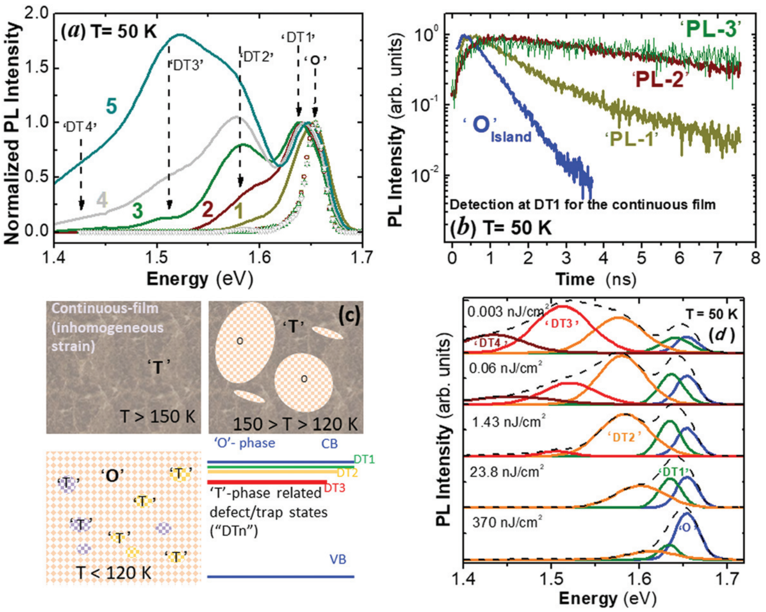

Fig. 3 (a) PL intensity depending on the bandgap energy (E_g) for five different fluence excitation conditions (curves 1: 370 nJ cm^{-2}, 2: 23.8 nJ cm^{-2}, 3: 1.43 nJ cm^{-2}, 4: 0.06 nJ cm^{-2} and 5: 0.003 nJ cm^{-2}) and for a temperature below the tetragonal–orthorhombic phase transition temperature (T = 50 K). Solid lines correspond to a 500 nm thick continuous-like sample, whereas scattered symbols correspond to the sample of the island-like film. The PL spectra were normalized at the highest PL peak energy line. (b) PL transients measured at the peak of the highest energy PL line. The blue line corresponds to the island-like film and the rest to the continuous-like sample at three different fluence excitation conditions. (c) Phenomenological scheme. (d) Gaussian fitting deconvoluted steady-state PL spectra profile of the continuous-like sample for five different fluence excitation conditions and at 50 K. Sub-band assignment: blue (orthorhombic, 'O'), green ('DT1'), orange ('DT2'), red ('DT3') and brown ('DT4').

increasing the laser excitation power. Phenomenologically, the observation of the 'DT'-band/s would be consistent with the state filling of a very broad energy spread of different energy levels below the 'O'-phase bandgap leading to carrier trapping. The physical origin of these levels would be found in locally defective 'T'-phase sites in the continuous sample, which can arise from strain inhomogeneities (different strain conditions at different size scales[12]), as compared to the case of the island-like sample. In this case, the strain conditions and inhomogeneities should be relaxed in a great part, because we observe a negligible contribution to PL on the low energy side of the 'O'-line peak (see Fig. 2d–f and 3a). If this is true, the behaviour of PL in the island-like sample at low temperatures would be similar to that expected in a single crystal of $MAPbI_3$. In fact, one can corroborate this asseveration by comparing the PL evolution in Fig. 2d–f with that in a good quality single crystal of $MAPbI_3$ in ref. 22. Moreover, the PL kinetics measured in the island-like sample is clearly associated with the 'O'-phase free exciton recombination, as discussed below.

As a consequence of the existence of 'DT'-levels, we observe that the intensity of the 'O'-line peak is practically constant in the island-like sample (Fig. 2d–f), whereas it increases until 100 K in the continuous film (Fig. 2a–c), just before the appearance of the 'T'-band. Moreover, the PL transients measured at the peak of the highest energy PL line (the 'O'-line peak in the island-like sample, but mixed 'O'-/'DT'-bands in the continuous-like one) are notably different in both samples (Fig. 3b). In the case of the island-like sample the PL decay is very fast (<1 ns) and independent of the excitation power, which can be associated with the free 'O'-exciton recombination, whereas it is slower when measured in the continuous-like sample, a signature of a recombination dynamics dominated by carriers trapped at 'DT'-levels and their connection with the 'O'-exciton recombination path. Therefore, the low temperature behaviour depicted here in the continuous sample is consistent with 'O'-phase $MAPbI_3$ with a certain energy distribution of shallow 'trap levels', whose possible origin would be the different strain conditions and different size scales of the strain inhomogeneities in the layer. These shallow 'trap levels' would be sequentially filled (from low to high energy) by increasing the laser excitation fluency (see Fig. 3a, where the low energy 'DT'-PL contribution grows in importance and shifts to the red by reducing the laser excitation power). By increasing the temperature (15–100 K), trapped electrons will be ionized towards the 'O'-phase conduction band. This carrier detrapping will partially restore the radiative exciton recombination channel, *i.e.*, will produce the observed intensity growth indicated above in the continuous-like sample.

Until now, it was shown that the orthorhombic phase could be stabilized through the effect of strain imposed on a thin film by the substrate[23,24] or through external pressure.[25] Now, we have introduced a new perspective. The existence of 'DT'-phases in the continuous-like morphology can be imagined as in the form of strained nanocrystals surrounded by 'O'-$MAPbI_3$. For this morphology, the PL from the 'O'-phase will be hidden at the lowest excitation powers (see the redshift of the highest energy PL line in Fig. 3a), where most of the photogenerated carriers are trapped at 'DT'-levels. On the other hand, in the island-like morphology, these 'DT'-phases are negligible because of strain relaxation of $MAPbI_3$-grains. For this morphology, the terms 'T'–'O' as crystallographic phases and 'T'–'O' in terms of optical transitions observed in PL have one-to-one correspondence. The origin of 'DT'-components of the PL spectra as arising from metastable 'T'-phase domains at the nanoscale would be also compatible with the presence of locally defective 'O'-phase sites due to locally different strain conditions. In any case, under both assumptions we would obtain the same observed emission phenomenology associated with radiative carrier trap levels.[26,27] The phenomenology depicted above when reducing the temperature from 300 to 15 K can be summarized in the illustration shown in Fig. 3c.

More quantitative information on the above-presented picture for recombination dynamics as a function of temperature in both morphologically different samples will be obtained after the appropriate deconvolution of their corresponding PL spectra recorded at several laser powers (Fig. 3d), especially in the case of the continuous-like sample, where several 'DT'-contributions are present. In fact, the 'O'-line peak energy extracted from the island-like sample will serve as a reference at every temperature, because it is independent of the excitation power (Fig. 3a), hence it can be fixed for the continuous-like sample, whose highest energy PL line is shifted to the red by reducing the laser fluency, by the influence of the shallowest 'DT'-levels, *i.e.*, the 'DT1'-contribution (green Gaussian PL line in Fig. 3d). From the multi-Gaussian fitting under different excitation powers at every temperature (Fig. 3d, as a low-T example, and Fig. S1† for the other powers and temperatures) we can extract the temperature evolution of the integrated intensities and peak energies for 'O'- and 'DTn'-components with temperature (Fig. S2 and S3,† respectively). From the temperature evolution of the PL integrated intensity (Fig. S2†) we corroborate our previous description: (i) the 'O'-related PL grows slightly with T in the range of 15–100 K, which is more important in the continuous-like sample at the expense of 'DTn'-deactivation, (ii) in the range of 120–150 K the 'O'-related PL intensity decreases, while the 'T'-related PL appears, and (iii) above 150 K the pure 'T'-related PL is recovered with an intensity value very similar to that measured when the pure 'O'-phase was dominating (≈100 K). Therefore, we can state that both 'O'- and 'T'-related PL lines are mainly due to radiative recombination until 200 K, approximately, above which the PL intensity of the 'T'-phase begins to decrease due to non-radiative recombination. Interestingly, the 'DTn'-related PL peak energy approximately follows the evolution found for the exciton recombination at the pure 'O'-phase, as observed in Fig. S3.† This observation points towards a behavior of 'DTn'-levels as determined by the 'O'-phase matrix, like nanocrystals (or QDs) of a different material with a different size and smaller bandgap (*e.g.*, like InGaAs QDs in GaAs matrix or core/shell nanocrystals).[28,29] The most likely possibilities, as pointed out above, continue to be locally defective 'T'-sites subjected to different strain conditions that affect the transition to the 'O'-phase, but also local 'T'- or 'O'-sites with different orientations of the $[CH_3NH_3]^+$ cation. In fact, the coexistence of crystallographic phases[30–32] has been reported in numerous inorganic perovskite materials.[23–25,33–35]

Now we can discuss more details of the recombination dynamics for the above-described optical transitions ('T', 'O' and 'DT*n*') in both samples in their corresponding range of temperature. For this, it will be interesting to compare the deduced PL decay times with the slopes deduced from the power dependence of PL intensity at different temperatures (see an example of the corresponding linear fittings in Fig. S4†), as summarized in Fig. 4a–d for the island-like and continuous-like samples, because we will obtain a very interesting correlation on the nature of the carrier recombination dynamics. PL decay times were obtained from single exponential fits to measured PL transients, as those shown in Fig. 3b. As a reference, in the island-like sample where the 'O'-phase is dominant, we observe a decay time of around 400 ps at 15 K that increases up to 2 ns at 120 K (Fig. 4a), which does not depend appreciably on the excitation power. At the same time, the slope associated with the power dependence of the PL intensity in the same temperature range is very close to unity (Fig. 4b). The latter observation tells us that free exciton (or correlated electron–hole) recombination is the main PL decay mechanism in the 'O'-phase of $MAPbI_3$, which is dominant in the island-like sample:[36–40]

$$\frac{dN_X}{dt} = -\frac{N_X}{\tau_X}.$$

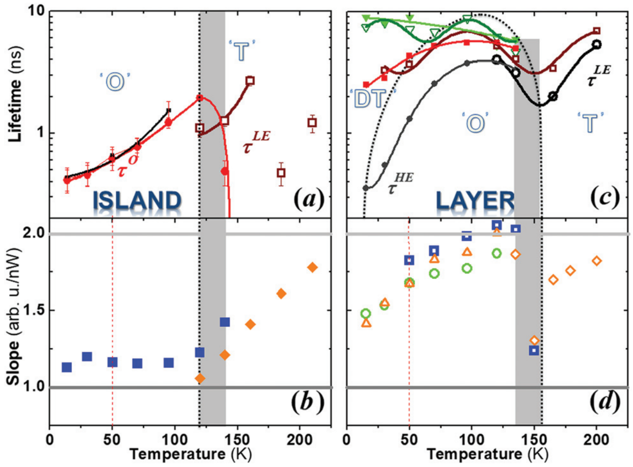

Fig. 4 Temperature evolution of the PL decay time measured in the island-like sample (a) and the continuous-like sample (c) at different excitation fluencies (circles: 370 nJ cm^{-2}, squares: 23.8 nJ cm^{-2}, triangles: 1.43 nJ cm^{-2}). Solid (open) symbols stand for decay times measured at the highest (lowest) PL peak energy; the lowest PL peak energy would correspond to 'DT2′-related emission, whereas the highest PL peak energy would correspond to mostly 'O'-related emission under the highest excitation fluency (370 nJ cm^{-2}) and mostly 'DT1′-related emission under the lowest excitation fluency (1.43 nJ cm^{-2}). (b) and (d) correspond to the temperature variation of the slopes extracted from the power dependence of the PL intensity for the island-like and continuous-like samples. A key to any symbol in these plots is provided: solid squares and different open symbols are used for the PL intensity-*vs.*-power slopes of the 'O'- and 'DT*n*'-related emission.

The first observation corroborates and complements this statement, given that the free exciton lifetime should increase with temperature due to the increased average kinetic energy of the exciton center-of-mass, as observed in other semiconductors with low density of impurities that impede bound exciton recombination.[41] Furthermore, the fast exciton lifetime measured in the 'O'-phase of $MAPbI_3$ reflects a huge oscillator strength in this material, but in the order of other direct bandgap semiconductors.[41] Given the large exciton binding energy of $MAPbI_3$ below T_C ('O'-phase), which is near 30 ± 5 meV,[9] there is a negligible contribution of free carriers in thermal equilibrium with excitons contributing to recombination, under (reasonably) low excitation power conditions. This behavior (free exciton recombination) is also possible because of the referred negligible contribution of 'DT'-levels to PL. At temperatures above 140 K, the slope of PL intensity *vs.* power begins to increase monotonically (≈1.75 at 200 K), as observed in Fig. 4b. This behavior would be associated with the growing importance of the bimolecular mechanism due to exciton dissociation (*i.e.*, higher proportion of free carriers in thermal equilibrium with excitons), now possible because of the reduction in the exciton binding energy above T_C ('T'-phase), which is 13 ± 5 meV:[9]

$$\frac{dn}{dt} = -Bn^2.$$

For the case of the continuous-like sample (Fig. 4c and d) the situation is more complex, because of the presence of 'DT*n*' contributions to PL below 100 K, especially at lower excitation powers. A general picture of most of the mechanisms explaining carrier recombination dynamics in $MAPbI_3$ (and other semiconductors) can be found in ref. 42, except non-radiative ones (Auger and Shockley–Read–Hall) that only play an important role above 200 K and under very high laser fluencies, out of our studied temperature and power ranges. The PL decay time measured at the highest PL peak energies (associated with the 'O'-phase, dominant at the highest excitation power, or with the 'DT1'-states, dominant at lower excitation powers) increases with decreasing excitation power (solid symbols in Fig. 4c). This time decay is similar to the 'DT2'-states (hollow symbols in Fig. 4c). At the same time, the slopes of the PL intensities (for the 'O'-exciton and 'DT*n*'-states) *vs.* power vary from 1.5 to 2 in the range of 15–150 K (Fig. 4d), which means that recombination, given that it is predominantly radiative, mainly originates from nongeminate (uncorrelated) instead of geminate (correlated) electron–hole formation of excitons at the 'O'-phase. That is, photogenerated electron–hole pairs at an energy level much higher (3.06 eV) compared to the 'O'-phase bandgap (≈1.66 eV) are being distributed among the different 'DT*n*'-levels and 'O'-excitons by carrier trapping/detrapping, hence avoiding a geminate formation of 'O'-excitons, as the dominant mechanism in the island-like sample. In spite of this formation origin of 'O'-excitons in the continuous-like sample, their lifetime, as measured at the PL peak energy under the highest excitation power (black solid circles in Fig. 4a), where most of the 'DT*n*'-states are being filled, is very similar and exhibits a similar temperature dependence to the lifetime for 'O'-excitons formed geminately in the island-like sample (solid symbols for two different excitation powers in Fig. 4a).

It is also interesting to highlight that the measured PL decay times for the 'O'-phase (below T_C) and 'T'-phase (above T_C) decrease when approaching T_C, as indicated by the continuous lines (a guide for the eyes) in Fig. 4a–c. This effect is associated with the intensity drops for both phases (Fig. S2†) when they are coexisting and appearing/disappearing. Therefore, it is clear that optical data allow a reliable comparison with structural ones. Again, if we compare the results obtained in X-rays by Weller *et al.*[45] with the analysis made from our PL measurements (continuous wave and time resolved) for the island-like sample, we observe many similarities:

(a) First, and independently of the fluence-excitation, we found that the orthorhombic phase is stable and exists alone for temperatures below 100 K, while the tetragonal phase is stable and exists alone for temperatures above 160 K and both are coexisting in between these temperatures, as it was discussed above and illustrated in Fig. 3c. This nearly pure 'O'-phase at low temperatures has not been reported previously in $MAPbI_3$ and, as demonstrated in this work, it is due to the morphology in the form of 1 μm size isolated islands, where crystalline grains can partially relax their strain during the island formation, as occurs in the case of the perovskite powder for which the X-ray diffraction study was carried out.[43]

(b) Secondly, the linewidth of the perovskite PL line can be strongly linked to the disorder in the orientation of the cation MA^+, while the existence of the 'O'-phase PL line is associated with and accounts for the distortion of the anion $[PbI_3]^-$. Specifically, at low temperatures, the frozen orientation of the MA^+ cation would be mostly ordered, which can be the reason for a very narrow PL linewidth (15 meV), as observed in Fig. S5.† In contrast, in the tetragonal phase, stable between 165 K and 327 K, the MA^+ cation is disordered over four sites directed toward the faces of the distorted cubic $[PbI_3]^-$ framework and migrates towards the cavity centre with increasing temperature. As a result, the linewidth of the 'T'-phase emission line is clearly much broader, near 50 meV at 200 K (Fig. S5†).

Therefore, our optical results for $T > 70$ K match the X-ray diffraction observations[43–45] and complete the structure picture expected below 70 K.

4. Conclusions

Morphological differences between samples (continuous-like and island-like) influence the optical properties and recombination dynamics with temperature. While continuous films exhibit strain inhomogeneities, this strain is relaxed in island-like samples. The PL spectra and carrier dynamics at low temperatures in the continuous-like sample are consistent with carrier trapping by energy levels extended more than 200 meV below the dominant orthorhombic, 'O'-phase bandgap. Contrarily, this effect is practically absent in strain-relaxed island-like films, where a single PL line is mainly observed at low temperatures that is associated with the 'O'-phase exciton recombination. Such an important difference between both sample morphologies would allow one to attribute carrier trapping levels to defective tetragonal, 'T'-phase sites in the continuous-like sample of $MAPbI_3$ (standard polycrystalline thin films usually prepared by wet chemistry for the fabrication of solar cells and other optoelectronic devices). These defective 'T'-phase sites can originate under different strain conditions at different size scales due to multiple twin domains with different frozen orientations of the MA^+ cations. Additionally, the recombination dynamics in the continuous-like sample is more complex than the free exciton recombination of the island-like sample, because of the presence of such defect/trap contributions ('DT*n*') to PL below 100 K, especially at lower excitation powers. Although it is predominantly radiative until 200 K, it mainly originates from nongeminate (uncorrelated) electron–hole formation of excitons at the 'O'-phase. This work suggests that strain inhomogeneities can influence the performance of the perovskite properties with an ulterior effect on the optoelectronic device performance. Our study points to the elimination of strain inhomogeneities as a fundamental way to reduce the presence of carrier trapping centres below the bandgap and hence a basis to obtain high-performance optoelectronic, photonic and plasmonic devices based on halide perovskites.

Conflicts of interest

There are no conflicts to declare.

Acknowledgements

This work has received funding from the European Union's Horizon 2020 research and innovation programme under the Marie Sklodowska-Curie grant agreement no. 704998 (RCJ). Financial support from the Spanish MINECO (projects TEC2017-86102-C2-1-R/2-R), Generalitat Valenciana (Q-Devices project Prometeo/2018/098) and Junta de Andalucía (PAI research group TEP-946) is acknowledged.

References

1 R. Chulia-Jordan and D. Santamaria-Perez, Four-mode plasmonic structure based on a prism-grating anticrossing bandgap, *Appl. Phys. Lett.*, 2012, **100**, 063301.

2 R. Chulia-Jordan and D. Santamaria-Perez, Tuning the propagation constant by the anticrossing bandgap prism coupling technique, *Plasmonics*, 2012, **7**, 665–675.

3 R. Chulia-Jordan and A. Unger, Comparison of the different bandgap cavities in a metallic four-mode plasmonic structure, *Plasmonics*, 2015, **10**, 429–438.

4 I. Suárez, E. J. Juarez-Perez, J. Bisquert, I. Mora-Seró and J. P. Martínez-Pastor, Polymer/perovskite amplifying waveguides for active hybrid silicon photonics, *Adv. Mater.*, 2015, 6157–6162.

5 S. D. Wolf, J. Holovsky, S.-J. Moon, P. Löpert, B. Niesen, M. Ledinsky, F.-J. Haug, J.-H. Yum and C. Ballif, Organometallic halide perovskites: Sharp optical absorption edge and its relation to photovoltaic performance, *J. Phys. Chem. Lett.*, 2014, **5**, 1035–1039.

6 D. L. Staebler and C. R. Wronski, Reversible conductivity changes in discharge-produced amorphous Si, *Appl. Phys. Lett.*, 1977, **31**, 292–294.

7 M. Stutzmann, W. B. Jackson and C. C. Tsai, Light-induced metastable defects in hydrogenated amorphous silicon: A systematic study, *Phys. Rev. B: Condens. Matter Mater. Phys.*, 1985, **32**, 23–47.

8 J. Even, L. Pedesseau and C. Katan, Analysis of multivalley and multibandgap absorption and enhancement of free carriers related to exciton screening in hybrid perovskites, *J. Phys. Chem. C*, 2014, **118**, 11566–11572.

9 R. Chulia-Jordan, E. Mas-Marza, A. Segura, J. Bisquert and J. P. Martínez-Pastor, Crystalline-size dependence of dual emission peak on hybrid organic lead iodide perovskite films at low temperature, *J. Phys. Chem. C*, 2018, **122**, 22717–22727.

10 K. Wu, A. Bera, C. Ma, Y. Du, Y. Yang, L. Li and T. Wu, Temperature-dependent excitonic photoluminescence of hybrid organometal halide perovskite films, *Phys. Chem. Chem. Phys.*, 2014, **16**, 22476–22481.

11 C. Wehrenfennig, M. Liu, H. J. Snaith, M. B. Johnston and L. M. Herz, Charge carrier recombination channels in the low-temperature phase of organic-inorganic lead halide perovskite thin films, *APL Mater.*, 2014, **2**, 081513.

12 T. W. Jones, A. Osherov, M. Alsari, M. Sponseller, B. C. Duck, Y. Jung, C. Settens, F. Niroui, R. Brenes, C. Stan, Y. Li, M. Abdi-Jalebi, N. Tamura, J. E. Macdonald, M. Burghammer, R. Friend, V. Bulovic, A. Walsh, G. J. Wilson, S. Lilliu and S. D. Stranks, Lattice strain causes non-radiative losses in Halide perovskites, *Energy Environ. Sci.*, 2019, **12**, 596–606.

13 G. Muñoz-Matutano, D. Barrera, C. R. Fernandez-Posa, R. Chulia-Jordan, L. Seravalli, G. Trevisi, P. Frigeri, S. Sales and J. Martinez-Pastor, All-optical fiber hanbury brown & twiss interferometer to study 1300 nm single photon emission of a metamorphic InAs quantum dot, *Sci. Rep.*, 2016, **6**, 27214.

14 G. Muñoz-Matutano, D. Barrera, C. R. Fernandez-Posa, R. Chulia-Jordan, J. Martinez-Pastor, I. Gasulla, L. Seravalli, G. Trevisi, P. Frigeri and S. Sales, Parallel recording of single quantum dot optical emission using multicore fibers, *IEEE Photonics Technol. Lett.*, 2016, **28**, 1257.

15 W. Kong, Z. Ye, Z. Qi, B. Zhang, M. Wang, A. Rahimi-Iman and H. Wu, Characterization of an abnormal photoluminescence behavior of perovskite $CH_3NH_3PbI_3$, *Phys. Chem. Chem. Phys.*, 2015, **17**, 16405.

16 R. Dhanker, A. N. Brigeman, A. V. Larsen, R. J. Asbury and N. C. Giebink, Random lasing in organo-lead halide perovskite microcrystal networks, *Appl. Phys. Lett.*, 2014, **105**, 151112.

17 T.-S. Kao, Y. H. Chou, C.-H. Chou, F.-C. Chen and T.-C. Lu, Lasing behaviors upon phase transition in solution-processed perovskite thin films, *Appl. Phys. Lett.*, 2014, **105**, 231108.

18 N. Fernández-Delgado, M. Herrera, F. J. Delgado, A. H. Tavabi, M. Luysberg, R. E. Dunin-Borkowski, E. J. Juárez-Pérez, B. Clasen Hames, I. Mora-Sero, I. Suárez, J. P. Martínez-Pastor and S. I. Molina, Structural characterization of bulk and nanoparticle lead halide perovskite thin films by (S)TEM techniques, *Nanotechnology*, 2019, **30**, 135701–135711.

19 C. Wehrenfennig, M. Liu, H. J. Snaith, M. B. Johnston and L. M. Herz, Homogeneous emission line broadening in the organo lead halide perovskite $CH_3NH_3PbI_3$-xClx, *J. Phys. Chem. Lett.*, 2014, **5**, 1421–1426.

20 Y. Yamada, T. Nakamura, M. Endo, A. Wakamiya and Y. Kanemitsu, Near-band-edge optical responses of solution-processed organic-inorganic hybrid perovskite $CH_3NH_3PbI_3$ on mesoporous TiO2 electrodes, *Appl. Phys. Express*, 2014, **7**, 032302.

21 H.-H. Fang, R. Raissa, M. Abdu-Aguye, S. Adjokatse, G. R. Blake, J. Even and M. A. Loi, Photophysics of organic-inorganic hybrid lead iodide perovskite single crystals, *Adv. Funct. Mater.*, 2015, **25**, 2378–2385.

22 M. Nagai, T. Tomioka, M. Ashida, M. Hoyano, R. Akashi, Y. Yamada, T. Aharen and Y. Kanemitsu, Longitudinal Optical Phonons Modified by Organic Molecular Cation Motions in Organic-Inorganic Hybrid Perovskites, *Phys. Rev. Lett.*, 2018, **121**, 145506.

23 R. J. Zeches, M. D. Rossell, J. X. Zhang, A. J. Hatt, Q. He, C.-H. Yang, A. Kumar, C. H. Wang, A. Melville, C. Adamo, G. Sheng, Y.-H. Chu, J. F. Ihlefeld, R. Erni, C. Ederer, V. Gopalan, L. Q. Chen, D. G. Schlom, N. A. Spaldin, L. W. MArtin and R. Ramesh, A strain-driven morphotropic phase boundary in BiFeO3, *Science*, 2009, **326**, 977–980.

24 Z. Chen, L. You, C. Huang, Y. Qi, J. Wang, T. Sritharan and L. Chen, Nanoscale domains in strained epitaxial BiFeO3 thin Films on LaSrAlO4 substrate, *Appl. Phys. Lett.*, 2010, **96**, 252903.

25 L. Ehm, L. A. Borkowski, J. B. Parise, S. Ghose and Z. Chen, Evidence of tetragonal nanodomains in the high-pressure polymorph of BaTiO3, *Appl. Phys. Lett.*, 2011, **98**, 021901.

26 V. S. Chirvony, S. Gonzalez-Carrero, I. Suarez, R. E. Galian, M. Sessolo, H. J. Bolink, J. P. Martinez-Pastor and J. Perez-Prieto, Delayed luminescence in lead halide perovskites nanocrystals, *J. Phys. Chem. C*, 2017, **121**, 13381–13390.

27 V. S. Chirvony and J. P. Martínez-Pastor, Trap-limited dynamics of excited carriers and interpretation of the

photoluminescence decay kinetics in metal halide perovskites, *J. Phys. Chem. Lett.*, 2018, **9**, 4955–4962.

28 N. S. Beattie, P. See, G. Zoppi, P. M. Ushasree, M. Duchamp, I. Farrer, D. A. Ritchie and S. Tomic, Quantum Engineering of InAs/GaAs Quantum Dot Based Intermediate Band Solar Cells, *ACS Photonics*, 2017, **4**, 2745–2750.

29 T. Sogabe, Q. Shen and K. Yamaguchi, Recent progress on quantum dot solar cells: review, *J. Photonics Energy*, 2016, **4**, 040901.

30 D. Santamaria-Perez and R. Chulia-Jordan, Compression of mineral barite, BaSO4: a structural study, *High Pressure Res.*, 2011, **32**, 81–88.

31 D. Santamaria-Perez, R. S. Kumar, A. J. Dos Santos-Garcia, D. Errandonea, R. Chulia-Jordan, R. Saez-Puche, P. Rodriguez and A. Muñoz, High-pressure transition to the post-barite phase in BaCrO4 hashemite, *Phys. Rev. B: Condens. Matter Mater. Phys.*, 2012, **86**, 94–116.

32 D. Santamaria-Perez, L. Gracia, G. Garbarino, A. Beltran, R. Chulia-Jordan, O. Gomis, D. Errandonea, Ch. Ferrer-Roca, D. Martinez-Garcia and A. Segura, High-pressure study of the behavior of mineral barite by X-ray diffraction, *Phys. Rev. B: Condens. Matter Mater. Phys.*, 2011, **84**, 054102.

33 S. Yokoyama, Y. Honda, H. Morioka, T. Oikawa and H. Funakubo, Large piezoelectric response in (111)-oriented epitaxial Pb(Zr,Ti)O3 films consisting of mixed phases with rhombohedral and tetragonal symmetry, *Appl. Phys. Lett.*, 2003, **83**, 2408–2410.

34 K. Saito, T. Kurosawa, T. Akai, S. Yokoyama, H. Morioka, T. Oikawa and H. Funakubo, Characterization of Epitaxial Pb(Zrx,Ti1-x)O3 Thin Films with Composition Near the Morphotropic Phase Boundary, *Mater. Res. Soc. Symp. Proc.*, 2011, **748**, DOI: 10.1557/PROC-748-U13.4.

35 M. Kelman, P. C. Mcintyre, B. Hendrix, S. Bilodeau, J. Roeder and S. Brennan, Structural analysis of coexisting tetragonal and rhombohedral phases in polycrystalline Pb (Zr0.35Ti0.65)O3 thin films, *J. Mater. Res.*, 2003, **18**, 173–179.

36 Y. Chen, T. Wang, Z. Li, H. Li, T. Ye, C. Wetzel, H. Li and S.-F. Shi, Communication Two States in Perovskite Revealed by Time-Resolved Photoluminescence Spectroscopy, *Sci. Rep.*, 2018, **8**, 16482.

37 L. H. Manger, M. B. Rowley, Y. Fu, A. K. Foote, M. T. Rea, S. L. Wood, S. Jin, J. C. Wright and H. Goldsmith, Global Analysis of Perovskite Photophysics Reveals Importance of Geminate Pathways, *J. Phys. Chem. C*, 2017, **121**, 1062–1071.

38 V. Sarritzu, N. Sestu, D. Marongiu, X. Chang, Q. Wang, M. A. Loi, F. Quochi, M. Saba and A. Mura, Perovskite Excitonics: Primary Exciton Creation and Crossover from Free Carriers to a Secondary Exciton Phase, *Adv. Opt. Mater.*, 2018, **6**, 1700839.

39 J.-C. Blancon, W. Nie, A. J. Neukirch, G. Gupta, S. Tretiak, L. Cognet, A. D. Mohite and J. J. Crochet, The Effects of Electronic Impurities and Electron-Hole Recombination Dynamics on Large-Grain Organic-Inorganic Perovskite Photovoltaic Efficiencies, *Adv. Funct. Mater.*, 2016, **26**, 4283–4292.

40 A. Dobrovolsky, A. Merdasa, E. L. Unger, A. Yartsev and I. G. Scheblykin, Defect-induced local variation of crystal phase transition temperature in metal-halide perovskites, *Nat. Commun.*, 2017, **8**, 34.

41 G. W. ‘t Hooft, W. A. J. A. van der Poel, L. W. Molenkamp and C. T. Foxon, Giant oscillator strength of free excitons in GaAs, *Phys. Rev. B: Condens. Matter Mater. Phys.*, 1987, **35**, 8281.

42 L. H. Manger, M. B. Rowley, Y. Fu, A. K. Foote, M. T. Rea, S. L. Wood, S. Jin, J. C. Wright and R. H. Goldsmith, Global Analysis of Perovskite Photophysics Reveals Importance of Geminate Pathways, *J. Phys. Chem. C*, 2017, **121**, 1062–1071.

43 I. P. Swainson, P. P. Hammond, C. Soullière, O. Knop and W. Massa, Phase transitions in the perovskite methylammonium lead bromide, $CH_3ND_3PbBr_3$, *J. Solid State Chem.*, 2003, **176**, 97–104.

44 A. Poglitsch and D. Weber, Dynamic disorder in methylammoniumtrihalogenoplumbates (II) observed by millimeter-wave spectroscopy, *J. Chem. Phys.*, 1987, **87**, 6373–6378.

45 M. T. Weller, O. J. Weber, P. F. Henry, A. M. Di Pumpo and T. C. Hansen, Complete structure and cation orientation in the perovskite photovoltaic methylammonium lead iodide between 100 and 352 K, *Chem. Commun.*, 2015, **51**, 4180–4183.